applied sciences

MDPI

Article

Degradation Mechanisms of Concrete in Underground Coal Mine Water Tanks Subjected to Sulphate Attack

Junliang Dong [1,2], Tao Han [3,*], Suo Zhang [1], Tingting Luo [3], Xiaobo Liu [1], Bing Xue [4], Yang Yan [1] and Yongsheng Ji [3]

[1] Shenhua Group Xinjie Energy Co., Ltd., Ordos 017200, China
[2] School of Mines, China University of Mining and Technology, Xuzhou 221116, China
[3] State Key Laboratory of Intelligent Construction and Healthy Operation and Maintenance of Deep Underground Engineering, China University of Mining and Technology, Xuzhou 221116, China
[4] Xuhai College, China University of Mining and Technology, Xuzhou 221008, China
* Correspondence: hantaocumt@163.com

Abstract

To simulate the partial immersion exposure typical of underground water storage, concrete specimens of different strength grades were partially submerged in Na_2SO_4 solution. Ultrasonic pulse velocity testing, microhardness measurements, and nanoindentation were employed to evaluate physical and micro-mechanical property degradation. In addition, the phase composition and content changes in different concrete regions using X-ray diffraction and thermogravimetric–differential scanning calorimetry are analysed to detect the time-varying phase compositions of concrete in various regions. The findings indicate that with the progress of corrosion, the overall infiltration of the wet area of C30 concrete tends to stabilize after attaining a certain height along the waterline. Subsequently, the corrosion solution gradually infiltrates and ascends along the concrete surface, leading to the overall breakdown and damage of the concrete within the climbing area from the water level line. In the corrosion and deterioration process of C40 concrete due to sulphate exposure, the corrosion solution gradually ascends from the concrete surface. The degree of surface degradation correlates with the height of the corrosion solution, eventually reaching the top of the concrete. As the sulphate surface climbing height increases, the ongoing alkali consumption reaction between the sulphate and the cement hydration product ultimately causes the fracture and decomposition of the cement stone structure.

Keywords: underground coal mine; water tank; concrete; sulphate attack; degradation mechanism

Check for updates

Academic Editor: Paulo Santos

Received: 8 September 2026
Revised: 21 October 2026
Accepted: 22 October 2026
Published: 26 October 2026

Copyright: © 2026 by the authors. Licensee MDPI, Basel, Switzerland. This article is an open access article distributed under the terms and conditions of the Creative Commons Attribution (CC BY) license.

1. Introduction

Water tanks in underground coal mines are typical deep underground concrete structures and an important part of the mine drainage system [1,2]. The main function of the water tank in underground coal mines is to store and settle mineral water. It can effectively buffer the fluctuation of the water inflow, ensure the stable operation of the drainage system under different working conditions, and is the key to preventing the occurrence of water disaster accidents [3,4].

As a major coal production hub in China, Inner Mongolia hosts extensive mining operations where shaft structures penetrate deep, water-rich sandstone formations. Groundwater within these deep strata typically carries high concentrations of aggressive ions, notably sulphate (SO_4^{2-}), which threaten the structural integrity of concrete water tank walls through severe degradation [5,6]. Ingress of sulphate ions via groundwater into concrete

tank linings induces cracking and localized matrix damage. Such structural degradation modifies the diffusion behaviour and concentration field of sulphates within the concrete, promoting secondary deterioration [7]. This synergistic coupling of chemical corrosion and physical damage progressively impairs water tank structural load-bearing capacity, posing a severe threat to operational safety.

The water tank is divided into three corrosion areas from the bottom to top, based on the differences in the corrosion environment: the fully immersed area, the wet area at the water level and the dry area [8–10]. Because sulphate corrosion in the wet areas at the water level is more severe than that in other areas, research on the sulphate corrosion of concrete in these wet areas has been a prominent topic of discussion. The current literature indicates that concrete degradation near the waterline is driven by physical and chemical sulphate attack, acting individually or synergistically [11–13]. The sulphate solution permeates the concrete and can react with the hydration product $Ca(OH)_2$ and aluminate compounds in the cement-based material, thus creating gypsum and calcite [14–16]. The accumulation of gypsum and calcite causes continuous expansion stress to the concrete pores, resulting in excessive local internal stress. Consequently, internal cracks within the concrete continue to expand, leading to more damage and deterioration, culminating in a progressive loss of structural strength and ultimate matrix collapse [17–19]. The physical corrosion caused by sulphate leads to the transmission of sulphate to the concrete surface via capillary pressure. Following sulphate evaporation on the concrete surface, the formation of supersaturated crystals causes the crystallisation pressure to exceed the ultimate tensile stress of the concrete pores, potentially damaging this area [20–22].

Currently, the protective measures against sulphate attack on concrete are mainly divided into three levels: material proportion, structural density, and surface protection [23,24]. Addition of mineral admixtures such as fly ash and slag can fill internal pores, refine pore size, and consume the easily erodible calcium hydroxide, thereby enhancing the resistance erosion. Controlling the water–cement ratio (water–binder ratio): reducing the water–cement ratio can reduce capillary pores and improve density, thus hindering the penetration sulphate solutions. Epoxy resin coatings are used to directly isolate the contact between sulphates and concrete. These measures play a certain protective role in the sulphate resistance of concrete, but their effect is limited, especially since epoxy resin coatings are prone to ageing and have a relatively short effective lifespan. In addition, it is known that sulphate ingress causes deterioration in the waterline wet zone, with the sulphate distribution range directly governing the extent of corrosion. Notably, surface tension induces continuous upward wetting on the concrete surface immediately above the waterline, forming an expanding erosion-wetting zone. This surface tension-driven infiltration phenomenon, however, is almost ineffective in preventing the surface migration of sulphates in this zone. This issue has received limited attention in previous partial-immersion sulphate.

To address this gap, we propose a novel “surface upward climbing coupled with downward alkali-consumption” degradation mechanism. Based on sulphate distribution, phase composition, and quantitative content analyses, we demonstrate that sulphate supersaturation in the waterline wet zone, sustained by continuous surface climbing, is the primary driver of its earlier onset, faster progression, and greater severity of deterioration compared to the submerged zone.

This study investigates the distribution of sulphate infiltration in different concrete samples of varying strength grades and the evolution of sulphate corrosion infiltration distribution in wet areas at the concrete water level. Furthermore, ultrasonic measurement, microhardness testing and nanoindentation methods were employed to examine the compactness and micro-nano-mechanical properties of the wet area at the concrete water level.

In addition, X-ray diffraction (XRD) and thermogravimetric-differential scanning calorimetry (TG-DSC) analyses were conducted to analyse the phase composition and content of concrete semi- immersed specimens in different areas and to assess the alterations in the phase composition of concrete in each area under sulphate semi-immersed corrosion.

2. Materials and Methods

2.1. Materials

This study used P·O 42.5 ordinary silicate cement, which meets the relevant requirements of "Common portland cement" (GB175-2023) [25] regarding its leading performance indicators. The fine aggregate used in the testing process was river sand with a well-distributed grade and a fineness modulus of 2.8, fulfilling the specifications outlined in the "Standard for Sand and Stone Quality and Inspection Methods for Ordinary Concrete" (JGJ52-2006) [26]. The stones used were continuously graded gravel with dimensions of 5~20 mm. They met the leading performance indicators according to the "Standards for Sand and Stone Quality and Inspection Methods for Ordinary Concrete" (JGJ52-2006).

2.2. Preparation of Specimens

According to the "Standard for Testing Methods of Mechanical Properties of Ordinary Concrete" method, prismatic specimens with dimensions of 100 mm × 100 mm × 300 mm and strength grades of C30 and C40 were prepared separately. The concrete mix proportions are shown in Table 1.

Table 1. Concrete mix ratio.

Strength Grade	Water (kg/m^3)	Cement (kg/m^3)	Fine Aggregate (kg/m^3)	Coarse Aggregate (kg/m^3)	Compressive Strength (MPa)	
					3 d	28 d
C30	190	317	681	1194	19.3	39.2
C40	182	372	625	1202	26.8	50.5

2.3. Semi-Immersed Sulphate Attack Test

The C30 and C40 concrete specimens, subjected to standard curing for 28 days, were immersed in Na_2SO_4 solution with a mass percentage concentration of 5% for semi-immersed corrosion experiments. The temperature and atmospheric relative humidity during the test were controlled at 20 ± 2 °C and 70 ± 5%, respectively. The sulphate solution is replaced once a week.

The liquid level of each solution was maintained at the height of 100 mm, approximately one-third of the total specimen height. During the experiment, regular replenishment was conducted to ensure the constancy of the solution's liquid level. The study included periodic assessments of changes in internal concrete infiltration, ultrasonic sound velocity tests, SO_4^{2-} distribution change characteristics, micro–nano mechanical alterations, and the physical phase of corrosion products at various locations within the C30 and C40 concrete specimens.

2.4. Experimental Research Content

2.4.1. Wetting Range of the Wet Area on the Water Level Line and the Law of SO_4^{2-} Wetting Climbing

(1) Humidity evolution process in the humid area on the water level line

The specimens of C30 and C40 concrete were removed regularly, cut along the centre of the specimens, and then photographed and observed in the interior with a digital camera (EOS R5 Mark II, Canon, Tokyo, Japan). The dry and wet areas inside the concrete were

divided by marking the infiltration range of the cut section, and the internal infiltration distribution of the concrete for C30 and C40 concrete specimens was documented at 1 month, 3 months, 6 months, 9 months and 12 months, respectively. The evolution law of sulphate infiltration in semi-immersed concrete was then studied.

(2) SO_4^{2-} infiltration climbing pattern in the wet area on the water level line

The C30 and C40 concrete specimens were retrieved after the corresponding corrosion period. The powder samples were extracted from the positions at 0 mm, 50 mm, 100 mm, 150 mm, 200 mm and 300 mm along the central axis of the specimen, as well as at 20 mm and 40 mm on both sides, located within the soaking area of the specimen at heights of 0 mm, 50 mm, 100 mm, 150 mm, 200 mm and 300 mm. The SO_4^{2-} content of concrete powders at different locations was analysed following the "Determination of Sulfate by General Test Method for Salt Industry" (GB/T13025.8-2012) [27]. The distribution of SO_4^{2-} content in C30 and C40 concrete was monitored at 1 month, 3 months, 6 months, 9 months and 12 months. This analysis aimed to investigate the distribution of SO_4^{2-} content in concrete and explore the evolution patterns of sulphate corrosion in semi-immersed eroded concrete.

2.4.2. The Evolution Process of the Density of the Wet Zone on the Concrete Water Level Line

According to the "Technical Regulations for Detecting Concrete Defects by Ultrasonic Method" (CECS 21:2000) [28], the ultrasonic pulse velocity method was applied to assess the C30 and C40 concrete specimens immersed in a 5% Na_2SO_4 solution. The NM-4B non-metallic ultrasonic detector (Ditu Biotechnology Co., Ltd., Beijing, China) was used to measure the midpoints of two pairs of parallel test surfaces at 0 mm, 100 mm, 150 mm, 200 mm and 300 mm within the immersion area of the specimen. The average ultrasonic pulse velocity on each test surface was recorded as the representative velocity for that height. Subsequently, the changes in the ultrasonic pulse velocity of C30 and C40 concrete specimens were documented over periods of 1 month, 3 months, 6 months, 9 months and 12 months, with a focus on investigating the evolution of compactness within the wet area along the water level line of the concrete.

2.4.3. The Evolution Process of Micromechanical Properties in the Wet Zone on the Concrete Water Level Line

The HVS-1000A Vickers hardness tester (HVS-1000A, Jinan Huaheng Testing Technology Co., Ltd., Jinan, China) was used to evaluate the microhardness changes of C30 and C40 concrete specimens immersed in a 5 wt% Na_2SO_4 solution for 1 month, 3 months, 6 months, 9 months and 12 months to examine the degradation patterns of microhardness in the semi-immersed eroded concrete. Specimens that had undergone the corresponding corrosion period were cut along the centre, and the test heights of 50 mm, 150 mm and 250 mm from the bottom of the soaking area were selected. Test points at the same height of 0 mm, 20 mm and 40 mm from the central axis of the specimen were also selected. Before testing, a coring machine extracted drill cores in a diameter range of 2 mm near each test point. The test surface of the sample and the corresponding back surface were polished using a series of sandpapers (600#, 800#, 1000#, and 1500#) before testing.

2.4.4. Micromechanical Properties and Component Transformation Process of Cementitious Structure

(1) Sample Preparation

The specimens subjected to the corresponding corrosion period were cut along the centre. A test height of 110 mm from the bottom of the specimen was then selected. A

10 mm cube was cut inward from the concrete surface at the test height, and a section parallel to the concrete was chosen as the sample's test surface and support surface. The test surface and the corresponding back surface were polished using a series of sandpapers (ranging from 600# to 5000#) for nanoindentation testing to examine the micromechanical properties of the cementitious structure and the component transformation process.

(2) Sample Testing

To characterize the evolution of micromechanical properties at the sample's reaction front, nanoindentation measurements were performed at exposure intervals of 1, 3, 6, 9, and 12 months using an NHT2 nanoindentation tester (Anton Paar GmbH, Graz, Austria) produced by Anton Paar. A two-stage loading protocol was implemented: an initial cycle reaching a maximum penetration depth of 300 nm was applied to extract microstructural mechanical parameters, followed by a second cycle extending to a maximum depth of 1500 nm. A test grid measuring 180 μm × 180 μm was arranged inward from the sulphate corrosion end, with a total of 100 nanoindentation test points set for each sample at intervals of 20 μm.

2.4.5. Influence of Distribution Changes in the Humid Area on the Water Level on the Phase Composition

X-ray diffraction (XRD, D8 Advance, Bruker, Karlsruhe, Germany) and thermogravimetric-differential scanning calorimetry (TG-DSC, STA 449 F3, Netzsch, Selb, Germany) analyses were conducted on powder samples obtained from various locations as specified in Section 2.4.2 to investigate the phase evolution process of semi-soaked eroded concrete in the transition zone between wet and dry areas. The positions of 50 mm, 150 mm and 250 mm from the bottom of the soaking area were selected as the test heights, with corresponding test points at the same heights and 40 mm from the central axis of the specimen. Changes in the corrosion products of the C30 and C40 concrete specimens were documented at intervals of 1 month, 3 months, 6 months, 9 months and 12 months during the semi-immersed corrosion of the concrete.

XRD Testing Procedure

During sample preparation, the test sample and corundum powder with 100% crystallinity were mixed and ground in anhydrous ethanol at a mass of 8:2, then dried in a fume hood before XRD testing. During testing using an XRD analysis instrument data were collected within a 2θ range of 3~0° with a 7 s/step time and a step size of 0.03°. The International Centre for Diffraction Data PDF-4 200 database was used, and DIFFRAC Eva 14 software was employed for qualitative phase identification search and matching. XRD Rietveld refinement, quantitative analysis, and data calibration completed using Topas Version 3 (Bruker AXS, Karlsruhe, Germany, 2004) software.

TG-DSC Testing Procedure

Linn High Therm GmbH VMK 1400 laboratory furnace is used for calcination of both raw materials and intermediate products, and the samples are kept in an alumina crucible and heated to the required temperatures. The samples are prepared in powder/pellet forms for the microanalytical study.

Simultaneous thermal analyses, thermogravimetric–differential thermogravimetric –differential thermal analysis (TG-DTG-DTA) with Proteus software (Version Proteus 5.2.1)., are used with alumina crucible fitted with pierced lids. The samples are used in powder form with size less than 25 mm for conducting thermal analysis to identify the phase transition temperature at a uniform heating rate of 10 C/min under nitrogen atmosphere.

For statistical decomposition of the nanoindentation data, the elastic modulus values obtained from the 100 indentation points per sample were compiled into frequency distribution histograms. These histograms were then fitted using multiple Gaussian distribution functions, with the fitting constrained by the characteristic elastic modulus ranges for each phase: pores (<7 GPa), LD C-S-H (7–20 GPa), HD C-S-H (20–35 GPa), UHD C-S-H (35–50 GPa), and unhydrated cement clinker (>50 GPa). The relative volume fraction of each phase was determined by integrating the area under its corresponding Gaussian peak. This deconvolution approach has been widely adopted for quantitative microphase analysis of cementitious materials and provides a robust basis for evaluating the evolution of C-S-H gel phases under sulphate attack.

2.4.6. Experimental Repeatability and Statistical Analysis

To ensure the reliability and statistical significance of the experimental results, a total of 5 exposure time points (1, 3, 6, 9, and 12 months) were set for each of the two concrete grades (C30 and C40). For each strength grade at each exposure age, 3 independent prismatic specimens (100 mm × 100 mm × 300 mm) were prepared, yielding 15 independent specimens per concrete grade and 30 specimens in total.

For sulphate ion content determination, powder samples were drilled at specified heights (0, 50, 100, 150, 200, 300 mm) and lateral depths (0, 20, 40 mm) from each specimen. Three independent powder samples were extracted in parallel at each sampling point for chemical titration, and the final reported value represents the average of 9 measurements (3 specimens × 3 parallel samples). For ultrasonic pulse velocity testing, three measurements were taken at each specified height on each specimen, and the average was used as the representative value; thus, 9 data points were obtained per height from 3 specimens. For microhardness testing, 5 indentation points (spaced $\geq$ 10 μm apart) were arranged within each specific coordinate area to avoid strain-field interference, yielding 15 hardness data points per position from 3 specimens. For nanoindentation, a 180 μm × 180 μm grid with a 20 μm pitch containing 100 independent indentation points was used per sample to ensure statistical robustness. For XRD and TG-DSC analyses, each test was repeated to ensure reproducibility of diffraction peak intensities and thermogravimetric mass-loss patterns. These replicate numbers and sampling strategies provide a solid basis for the reported differences and conclusions.

3. Results and Discussion

3.1. Infiltration Evolution Process of the Wet Zone on the Water Level

(1) C30 concrete

Figure 1 shows the evolution process in the seepage of C30 concrete's Na_2SO_4 semi-immersed corrosion solution. This figure indicates that at a corrosion age of one month, the infiltration height of the corrosion solution in the concrete slightly exceeded the water level line, with a small accumulation of Na_2SO_4 crystals forming at the top of the infiltration zone. After three months of corrosion, the infiltration height on the surface of C30 concrete increases, with the liquid level of the corrosive solution becoming higher on the edges of the concrete section compared to the middle. At six months of corrosion, the overall height of the wet zone at the water level remained constant, and the corrosion solution continued its upward progression along the specimen's sides. This phenomenon is attributed to the limited overall ascent of the corrosive solution. It is affected by the wettability of the degraded and decomposed sludge on the concrete's lateral surfaces, thus facilitating the upward movement of the solution.

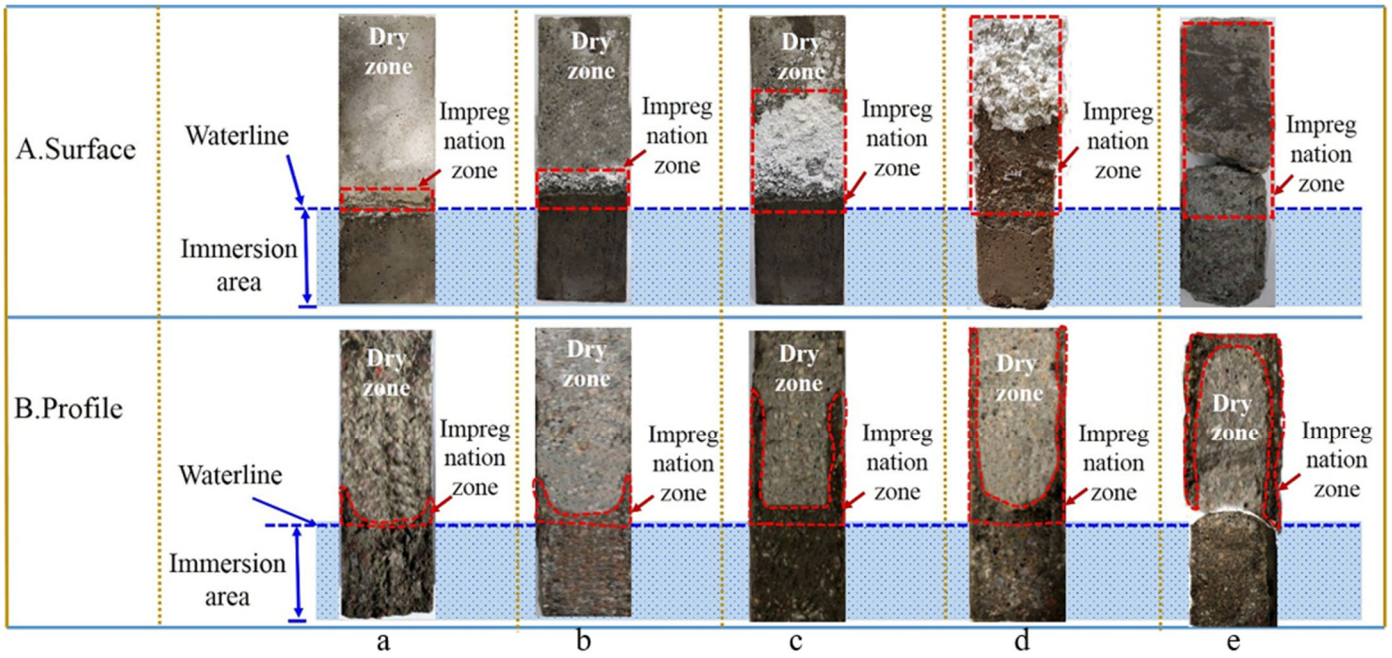

Figure 1. The evolution process in the seepage of C30 concrete's Na_2SO_4 semi-immersed corrosion solution. (**a**) 1month; (**b**) 3months; (**c**) 6months; (**d**) 9months; (**e**) 12months.

At nine months of corrosion, the wet zone's height at the water level remained constant, with the corrosion solution ascending along the sides of the specimen to its apex. At 12 months of corrosion, the specimen exhibited fracturing and decomposition starting from the wet zone at the water level. This phenomenon can be attributed to a higher sulphate concentration in the wet area above the water level than below it. Meanwhile, the corrosion solution in the regions that were distant from the water level only caused surface corrosion on the concrete without penetrating its interior. As the corrosion solution in the wet zone at the water level continued to infiltrate and expand internally, the alkali consumption deterioration reaction within the concrete intensified, ultimately causing the deterioration and decomposition of this area.

(2) C40 concrete

Figure 2 shows the evolution process in the seepage of C40 concrete's Na_2SO_4 semi-immersed corrosion solution. At one month of corrosion, the infiltration rate of the corrosion solution in the C40 concrete exceeded the water level. However, the solution only permeated the specimen's surface without penetrating the concrete. With the increase in the corrosion age, the corrosion solution progressively ascended toward the top of the specimen and infiltrated the concrete's interior. At nine months of corrosion, the corrosion solution had permeated the top of the specimen, resulting in a muddy and cracked surface. At 12 months of corrosion, muddiness and spalling on the top of the C40 concrete became more pronounced, with a substantial accumulation of Na_2SO_4 crystals. Although the corrosion solution infiltrated the concrete's interior, this infiltration remained confined to the surface layer, leaving the interior of the concrete dry.

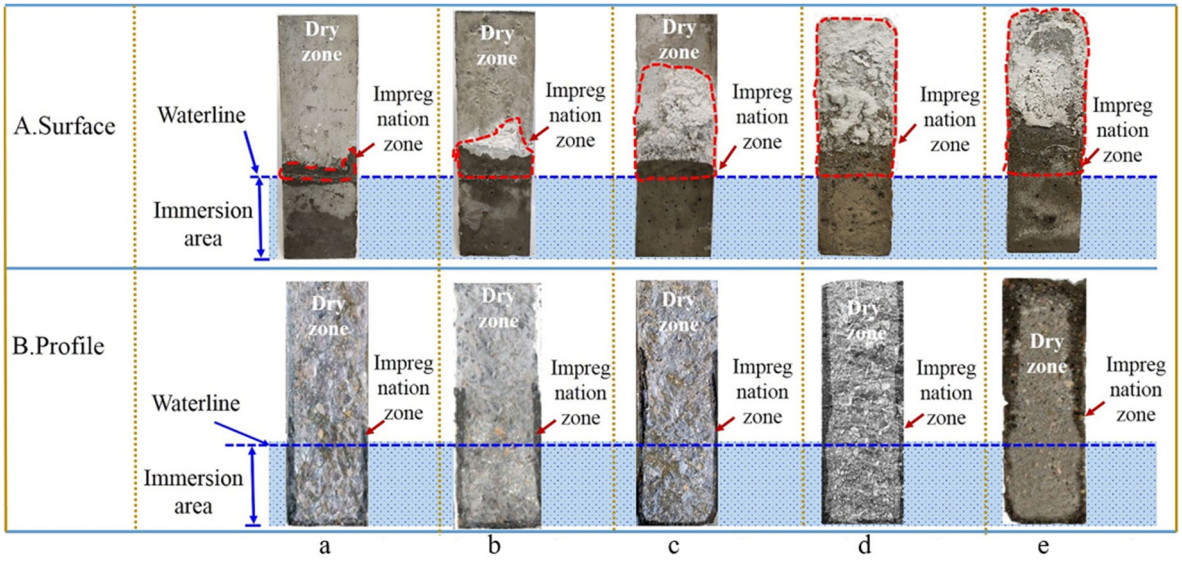

Figure 2. The evolution process in the seepage of C40 concrete's Na_2SO_4 semi-immersed corrosion solution. (**a**) 1month; (**b**) 3months; (**c**) 6months; (**d**) 9months; (**e**) 12months.

3.2. SO_4^{2-} Infiltration Climbing Pattern in the Wet Zone Above the Water Level

(1) C30 concrete

Figure 3 depicts the distribution of SO_4^{2-} across different regions of C30 concrete. In the absence of sulphate corrosion, the SO_4^{2-} concentration within the C30 concrete consistently remained within the range of 0.40~0.50%. This outcome indicates that the sulphur compound content inside the concrete stayed within a specific range.

At three months of corrosion, the SO_4^{2-} concentrations at 0 mm, 50 mm and 100 mm from the bottom of the concrete were 2.1–2.3%, 1.8–1.9% and 1.8–1.9%, respectively. At a distance of 150 mm from the bottom, the SO_4^{2-} contents at −40 mm, −20 mm, 0 mm, 20 mm and 40 mm along the X-axis were 1.75%, 1.12%, 0.61%, 1.01% and 1.90%, respectively. When the measurement was 200 mm from the bottom, the corresponding SO_4^{2-} contents were 0.91%, 0.51%, 0.52%, 0.92%, and 1.97%, respectively. At 300 mm from the bottom, the SO_4^{2-} levels at −40 mm, −20 mm, 0 mm, 20 mm and 40 mm along the X-axis were 2.09%, 0.94%, 0.52%, 0.52%, 0.95% and 2.02%, respectively. These findings indicated that the SO_4^{2-} concentration in the wet zone above the water level was primarily concentrated along the sides of the concrete. Sulphate was yet to permeate the interior of the concrete. Meanwhile, the sulphate content within the immersion zone of the concrete was relatively uniform.

At 12 months of corrosion, the SO_4^{2-} concentrations at 0 mm, 50 mm and 100 mm from the bottom of the concrete range between 2.51–2.78%, 2.45–2.81%, and 2.52–2.80%, respectively. This finding indicates that with an increase in the corrosion age, the SO_4^{2-} content in the immersion area of the concrete demonstrated an overall upward trend. However, the sulphate content gradually diminished from the surface towards the interior within the soaked area. The SO_4^{2-} levels at 100 mm, 200 mm and 300 mm from the bottom of the concrete fall within the ranges of 1.92–2.84%, 2.05–3.16% and 3.05–3.81%, respectively. This pattern indicates that as the age of corrosion progresses, the sulphate content in the wet zone at the water level steadily increases from the surface to the interior. Moreover, the sulphate concentration at the outer edge of the concrete's top was higher than that in other areas.

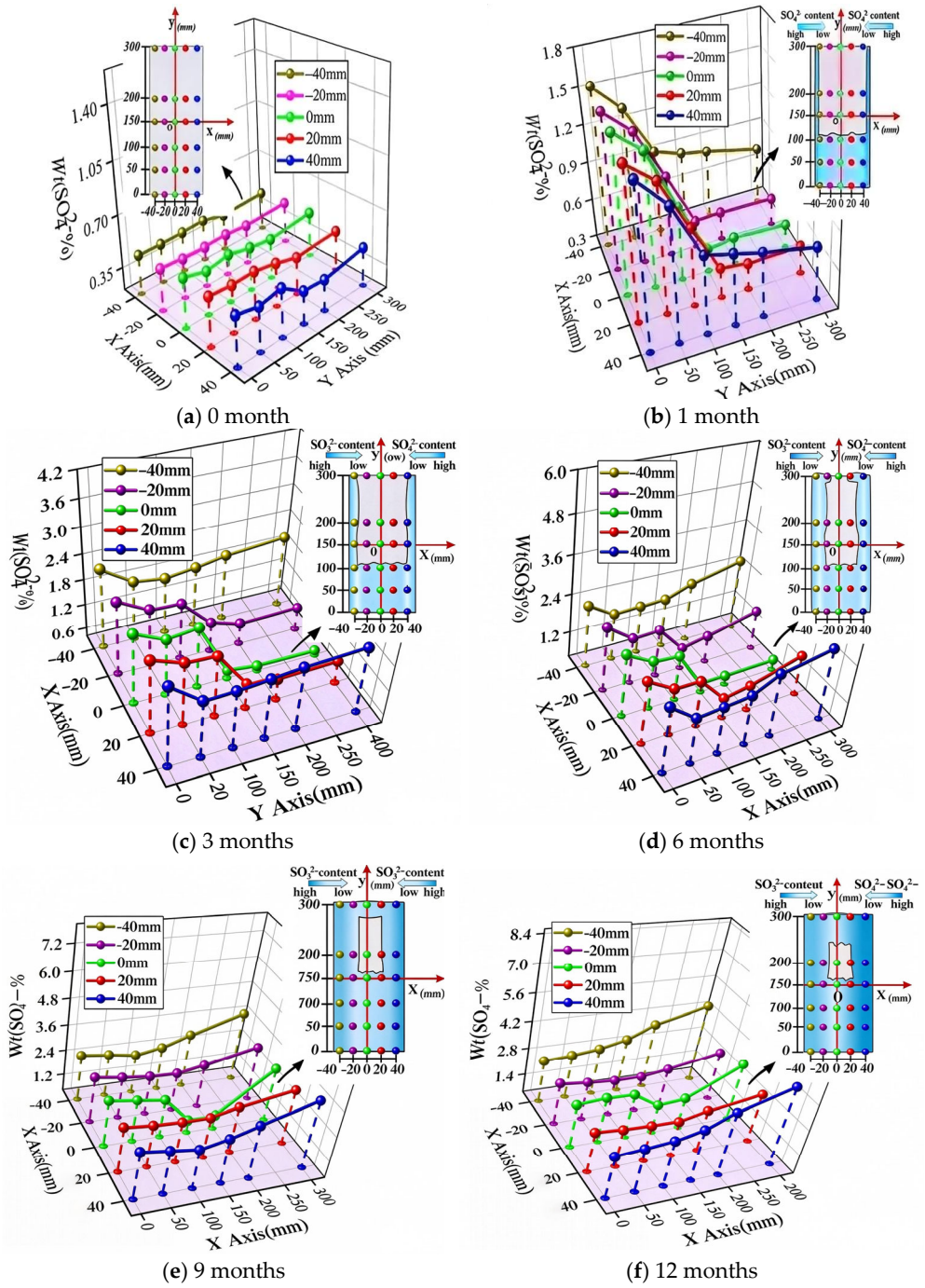

Figure 3. The distribution of SO_4^{2-} across different regions of C30 concrete.

(2) C40 concrete

Figure 4 shows the distribution of SO_4^{2-} across different regions of C40 concrete. At three months of corrosion, the SO_4^{2-} concentrations at 0 mm, 200 mm and 300 mm from the bottom of the concrete range between 0.49 and 0.56%, 0.47 and 0.50%, and 0.47 and 0.49%, respectively. At 50 mm, 100 mm, and 150 mm from the bottom, the SO_4^{2-} content within a horizontal span of 20 mm varies approximately from 0.48 to 0.50%. Similarly, at these heights (50 mm, 100 mm, and 150 mm), the SO_4^{2-} content at a horizontal distance of 40 mm from the central axis was also within the range of 0.48–0.50%. Furthermore, the SO_4^{2-} levels at 40 mm from the central axis at these heights were 0.59%, 0.76% and 0.46%, respectively.

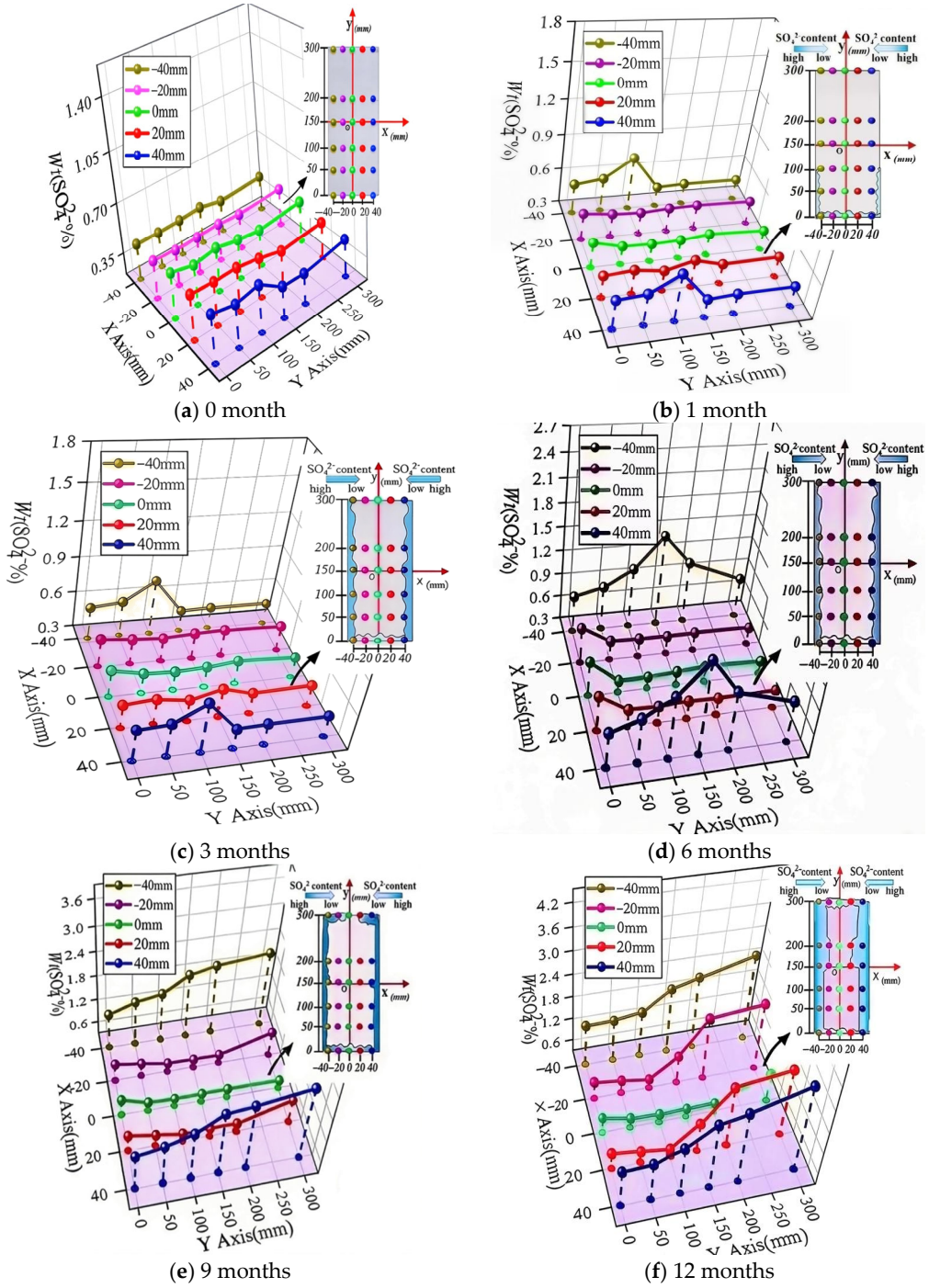

Figure 4. The distribution of SO_4^{2-} across different regions of C40 concrete.

At 12 months of corrosion age, the SO_4^{2-} concentrations at distances of −40 mm, −20 mm, 0 mm, 20 mm and 40 mm along the X-axis, 150 mm from the bottom of the concrete, were 2.09%, 1.09%, 0.52%, 1.07%, and 2.10%, respectively. At a vertical distance of 200 mm from the bottom of the concrete, the SO_4^{2-} levels at −40 mm, −20 mm, 0 mm, 20 mm and 40 mm along the X-axis were 2.22%, 1.93%, 0.51%, 1.90% and 2.18%, respectively. When measured 300 mm from the bottom of the concrete, the SO_4^{2-} concentrations at −40 mm, −20 mm, 0 mm, 20 mm and 40 mm along the X-axis were 2.61%, 2.09%, 1.03%, 2.12% and 2.56%, respectively.

3.3. The Evolution Process of the Density of the Wet Zone on the Concrete Water Level Line

Figure 5 shows the changes in the ultrasonic velocity of concrete half-immersed in the Na_2SO_4 solution. The figure revealed that in the absence of corrosion, the ultrasonic sound speeds in C30 and C40 concrete areas were maintained at 4.15–4.20 km/s and 4.24–4.30 km/s, respectively. At a corrosion age of 3 months, the ultrasonic sound velocities at heights of 0 mm, 100 mm, 150 mm, 200 mm and 300 mm for C30 concrete were recorded as 4.31 km/s, 4.33 km/s, 4.26 km/s, 4.24 km/s and 4.24 km/s, respectively. Meanwhile, the ultrasonic speed in C40 concrete remained within the range of 4.24–4.30 km/s.

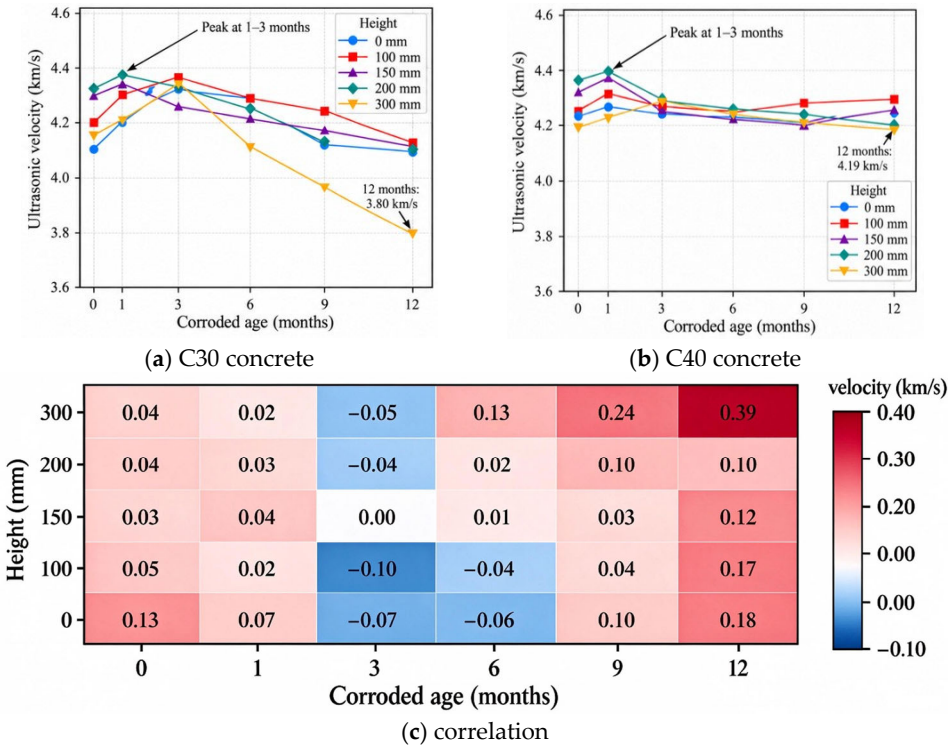

Figure 5. The changes in the ultrasonic velocity of concrete half-immersed in the Na_2SO_4 solution.

This result indicates that because of the lower density of C30 concrete, the Na_2SO_4 solution can rapidly permeate into the interior of the concrete, initiating a deterioration reaction. The resultant hydration products fill the internal pores, increasing the concrete specimen's density. Consequently, this outcome leads to an increase in the ultrasonic velocity rate in C30 concrete.

At 12 months of corrosion, the ultrasonic sound velocities in C30 concrete at heights of 0 mm, 100 mm, 150 mm, 200 mm and 300 mm were 4.15 km/s, 4.13 km/s, 4.26 km/s, 4.14 km/s and 4.04 km/s, respectively. For C40 concrete at similar heights of 0 mm, 100 mm, 150 mm, 200 mm, and 300 mm, the ultrasonic velocities were 4.27 km/s, 4.30 km/s, 4.22 km/s, 4.20 km/s, and 4.19 km/s, respectively.

The analysis reveals that the internal density of C40 concrete immersed in the Na_2SO_4 solution consistently exceeds that of C30 concrete. In the wet zone at the water level, the concrete density gradually decreases from lower to higher strengths; however, the overall density of medium-high strength concrete remains relatively unchanged. This finding indicates that in C30 concrete semi-immersed in the Na_2SO_4 solution, the immersion and wet zones at the water level experience concurrent deterioration and disintegration. However, in C40 concrete, the deterioration rate in the wet zone at the water level is more pronounced than in the immersion zone.

3.4. Evolution Process of Micromechanical Properties in the Wet Zone on the Concrete Water Level Line

(1) C30 concrete

Figure 6 shows the spatial microhardness distribution across C30 concrete sections. Unexposed specimens maintained a baseline internal microhardness of 63.5–64.1 HV. After 6 months of sulphate exposure, microhardness values across horizontal intervals of −40 to −20 mm, −20 to 0 mm, 0 to 20 mm, and 20 to 40 mm decreased to 61.0–62.6 HV, 62.6–63.1 HV, 62.0–63.1 HV, and 60.7–63.1 HV, respectively. When the corrosion age reached 12 months, the microhardness values in these respective horizontal intervals of the specimen were 48.2–55.6 HV, 55.6–60.5 HV, 55.7–61.6 HV, and 48.8–55.7 HV.

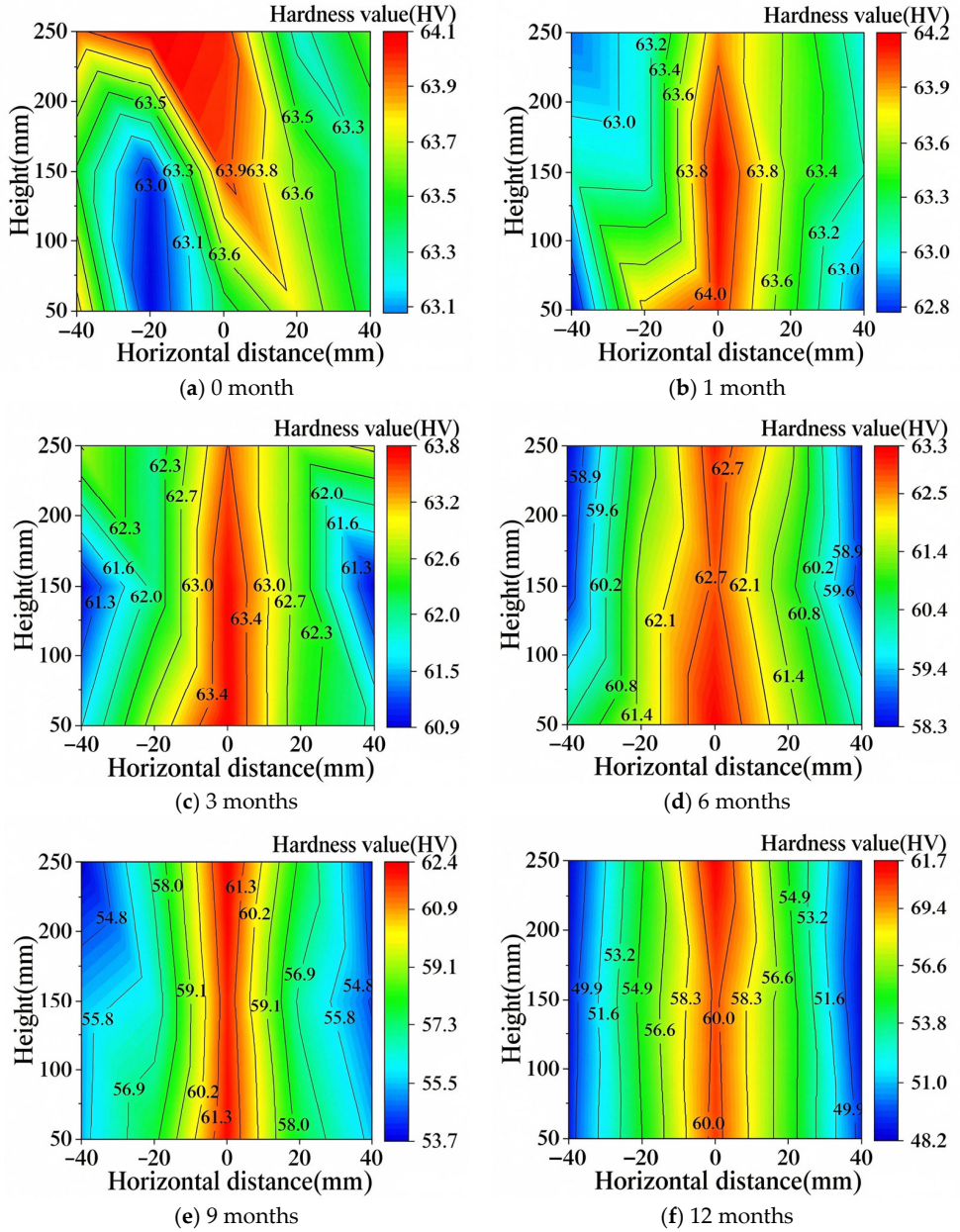

Figure 6. The distribution of microhardness in each area of C30 concrete.

The evaluation reveals consistent microhardness values in the symmetrical areas of the half-immersed Na_2SO_4 solution specimen. Notably, the microhardness near the specimen's axis (the −20 mm−20 mm area) consistently exceeded that in the concrete surface area. As the soaking age progressed, deterioration coincided from the surface to the interior in

the horizontal direction of the concrete, both in the wetted area at the water level and the soaked area. In the vertical direction, the wetted area at the water level of the concrete demonstrated more pronounced deterioration than the area immersed in the solution.

(2) C40 concrete

Figure 7 shows the microhardness distribution in different areas of C40 concrete. The figure demonstrates that in the absence of corrosion, the internal microhardness of the concrete specimen remained within a range of 67.0–67.6 HV. At a corrosion age of six months, the microhardness values in the horizontal direction of the specimen at intervals of −40–−20 mm, −20–0 mm, 0–20 mm, and 20–40 mm were 62.2–63.5 HV, 63.5–67.5 HV, 64.1–67.2 HV and 62.8–64.1 HV, respectively. At 12 months of corrosion, the microhardness values in these respective horizontal intervals of the specimen were 52.7–56.5 HV, 56.5–66.2 HV, 57.0–66.2 HV, and 52.2–57.0 HV.

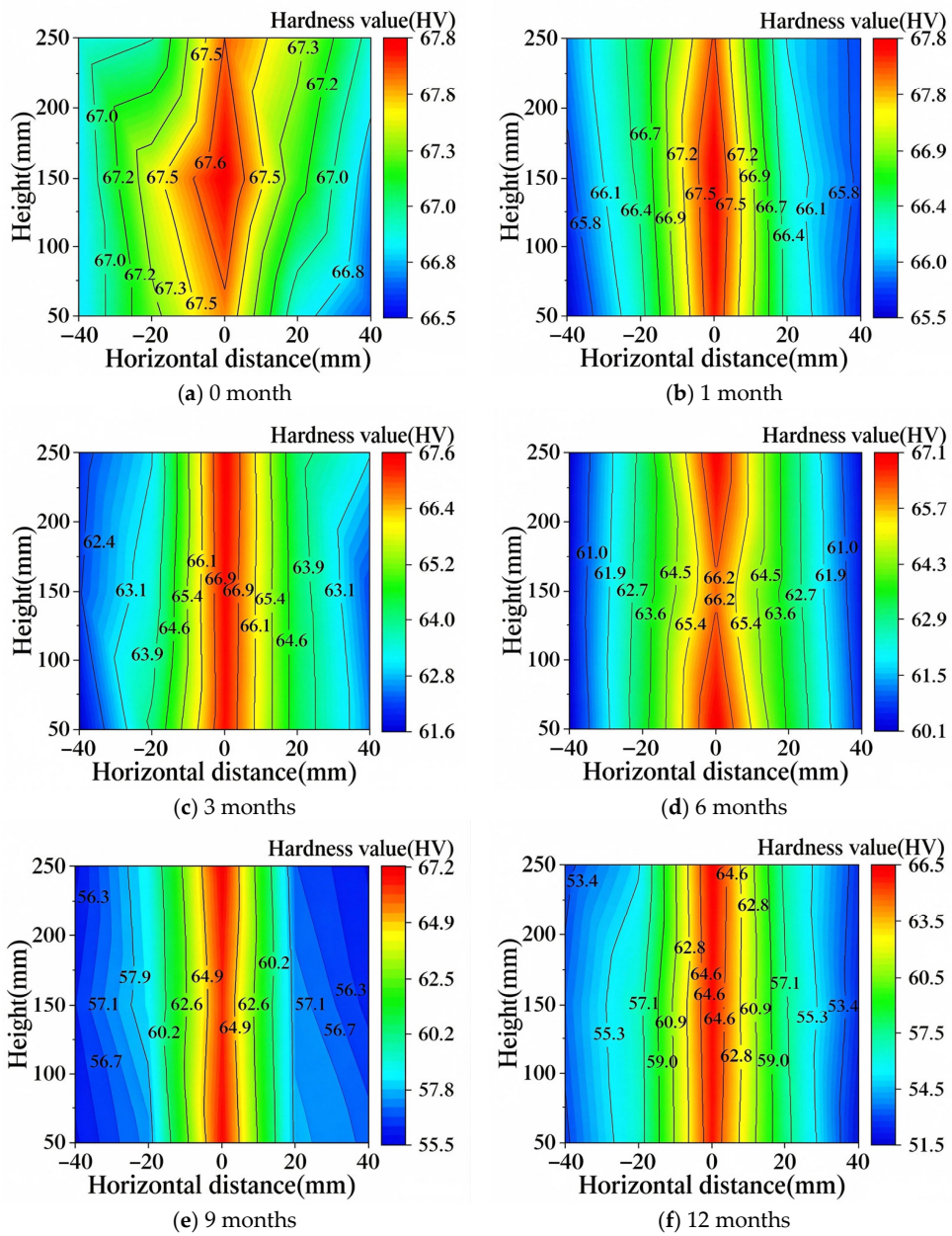

Figure 7. The microhardness distribution in different areas of C40 concrete.

The analysis indicates that with increasing corrosion age, the microhardness in the horizontal direction progressively increased from the exposed surface toward the specimen interior (i.e., it decreased from the centre toward the Na_2SO_4– exposed edges). Concurrently, the microhardness considerably increased from top to bottom in the vertical direction. This observation suggests that with the increased strength level of concrete, the Na_2SO_4 solution primarily causes corrosion damage to the surface of the semi-immersed concrete specimen. At the same time, the mechanical properties in most internal areas remained primarily unaffected by significant degradation. In addition, the extent of deterioration in the concrete above the liquid level, caused by Na_2SO_4, progressively intensified from bottom to top. Conversely, the degree of deterioration in the concrete below the liquid level was marginally less than that in the area above the liquid level.

3.5. The Micromechanical Properties and Component Transformation Process of the Cement Stone Structure

(1) C30 concrete

Figure 8 shows the elastic modulus distribution of C30 concrete corrosion. The elastic modulus distribution cloud map of the specimen includes areas ranging from 0–21 GPa (blue area), 21–42 GPa (green area), 42–49 GPa (yellow area) and 49–65 GPa (red area). According to the literature, the elastic modulus of pores is <7 GPa, the elastic modulus of low-density CSH gels (LD CSH) is 7–20 GPa, the elastic modulus of high-density CSH gels (HD CSH) is 20~35 GPa, the elastic modulus of ultra-high-density CSH gels (UHD CSH) is 35–50 GPa, and the elastic modulus of cement clinker is >50 GPa [29,30].

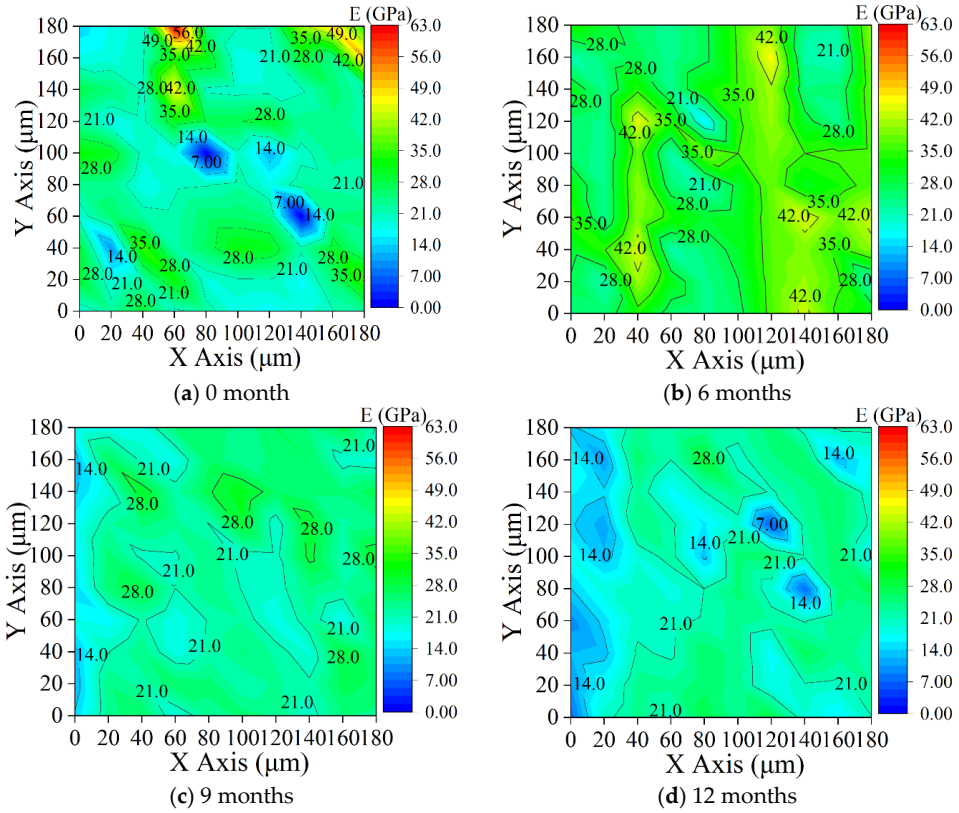

Figure 8. The elastic modulus distribution of C30 concrete corrosion. X-axis and Y-axis represent the planar coordinates of indentation points with the unit of μm.

The elastic modulus cloud map for the first six months of corrosion age indicates that the distribution of LD CSH gradually decreases with the increase in corrosion age. In contrast, the distribution of HD CSH and UHD CSH gradually increases. This result

suggests a gradual increase in the elastic modulus of the CSH gel at this stage, leading to an overall improvement in the strength of the cement stone structure.

Elastic modulus contour maps at 0, 6, 9 and 12 months of degradation reveal a progressive expansion of low-density C-S-H over time. This trend is particularly prominent adjacent to the reaction front, reflecting a broader spatial distribution across the matrix. Conversely, the distribution of HD CSH and UHD CSH gels gradually decreases. This outcome indicates that beyond a certain age, the elastic modulus of the CSH gel gradually decreases, causing an overall decline in the cement stone structure due to the insufficient resistance of the CSH gel.

Statistical analysis of the elastic modulus values derived from nanoindentation yields the phase frequency distribution for C30 concrete (Figure 9). Within the first 6 months of corrosion, the C30 concrete matrix was dominated by high-density (HD) and ultra-high-density (UHD) C-S-H gels. With prolonged exposure, low-density (LD) C-S-H became the predominant microstructural phase. This shift suggests that while initial hydration converts early-stage LD C-S-H into denser HD C-S-H, subsequent sulphate attack degrades these high-density phases, impairing the overall mechanical performance. Consequently, Na_2SO_4 ingress causes microstructural instability and matrix softening, primarily driven by the mechanical breakdown of C-S-H gel, the core binding component of cementitious materials.

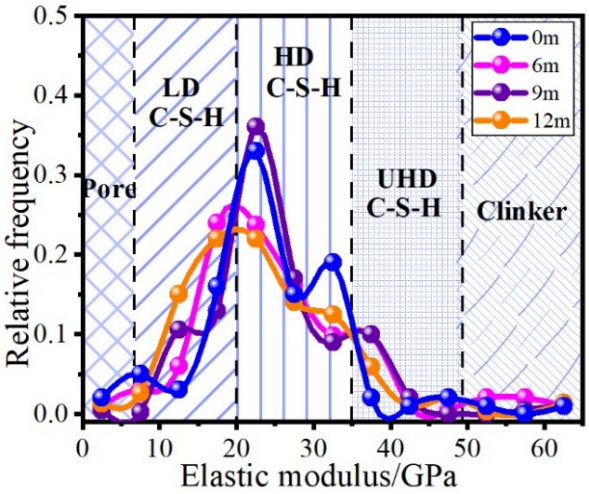

Figure 9. The frequency distribution of the nanoindentation results.

(2) C40 concrete

Figure 10 shows the elastic modulus distribution of C40 concrete corrosion. At a corrosion age of 0 months, the elastic modulus of the leading edge of C40 concrete reveals an even distribution of high-density CSH gel (green area) covering a wide range, with scattered low-density CSH gel (light blue area) and UHD CSH gel in the test area when there is no corrosion.

Figure 10b–d depicts the cloud diagram of the elastic modulus distribution at the leading edge of corrosion for the Na_2SO_4 specimen at corrosion ages of 6, 9 and 12 months. With an increase in the corrosion age, the elastic modulus at the leading edge gradually decreased from near to far. The distribution area of pores and LD CSH initially decreased, then increased. Meanwhile, the distribution area of HD CSH and UHD CSH first increased, then gradually decreased. This result indicates a decline in the overall strength of the CSH gel, the primary strength component of the cement-based material, with the progression of corrosion age.

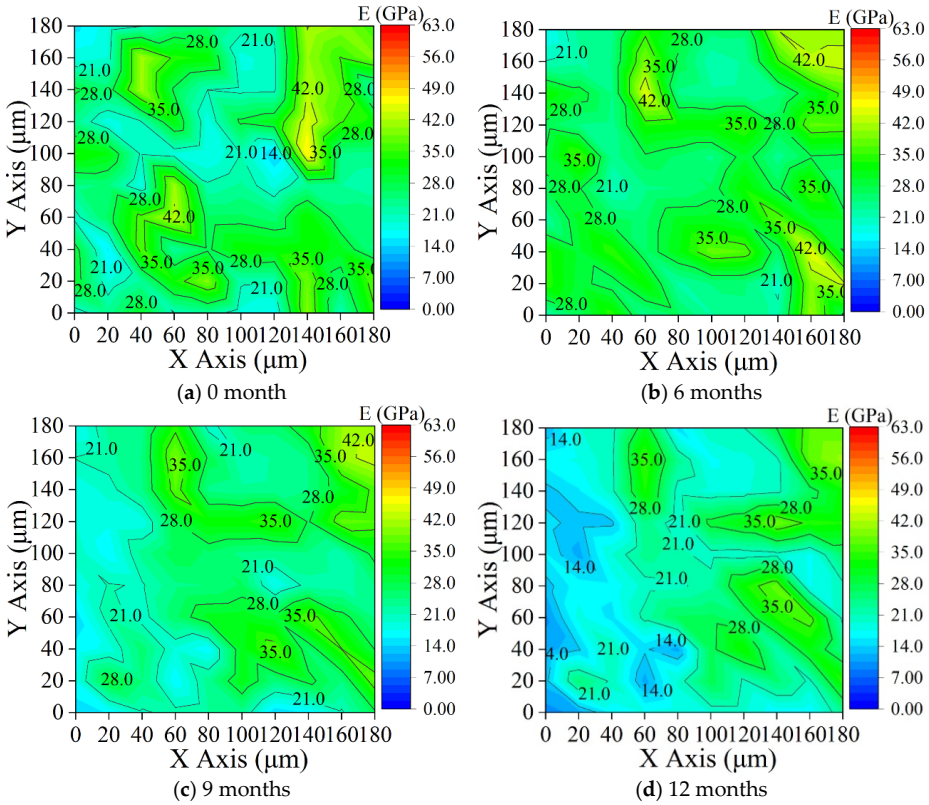

Figure 10. The elastic modulus distribution of C40 concrete corrosion. X-axis and Y-axis represent the planar coordinates of indentation points with the unit of μm.

Statistical evaluation of nanoindentation elastic modulus data yields the phase frequency distribution for C40 concrete at the reaction front (Figure 11). The elastic modulus is heavily concentrated in the HD C-S-H regime (20–35 GPa), confirming that C-S-H gel remains the primary load-bearing backbone of the cementitious matrix during Na_2SO_4 ingress. With prolonged exposure, the UHD C-S-H fraction decreases monotonically. Conversely, HD C-S-H exhibits a parabolic trend (an initial rise followed by a decline), whereas LD C-S-H shows the opposite profile (an initial decrease followed by a rebound). This dynamic shift underscores a progressive phase transition of C-S-H gel from high-density to low-density states as corrosion advances. Additionally, the rising pore fraction with exposure time suggests partial structural decomposition and decalcification of the C-S-H gel matrix.

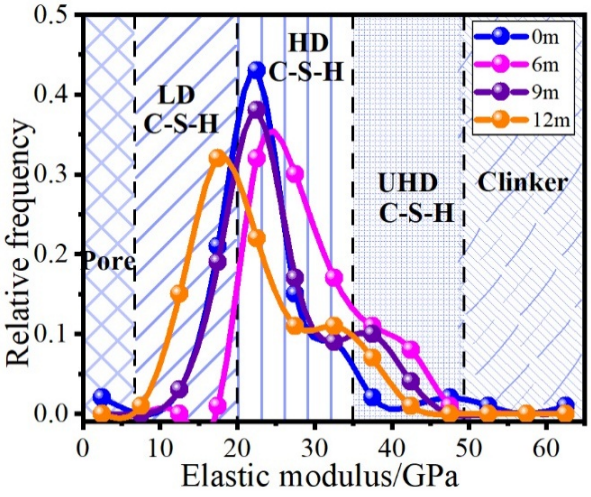

Figure 11. The frequency distribution of the C40 concrete nanoindentation results.

3.6. X-Ray Diffraction (XRD) Analysis

Figure 12 depicts the XRD analysis results for different areas of C40 concrete. The phase composition of C40 concrete, semi-immersed in a Na_2SO_4 solution, includes $Ca(OH)_2$: Portlandite (Calcium hydroxide, $Ca(OH)_2$) (PDF# 44-1481), AFm: Monosulphate phase (Aluminate-ferrite-monosulphate, $C_3A{\bullet}CaSO_4{\bullet}12H_2O$) (PDF# 44-0158), C_3AH_6: Hydrogarnet/Katoite (Tricalcium aluminate hexahydrate, $3CaO{\bullet}Al_2O_3{\bullet}6H_2O$) (PDF# 24-0217), CFH: Calcium ferrite hydrate (PDF# 21-0830), Aft: Ettringite (Aluminate-ferrite-trisulphate, $3CaO{\bullet}Al_2O_3{\bullet}3CaSO_4\ {\bullet}32H_2O$) (PDF# 41-1451), gypsum: Gypsum (Calcium sulphate dihydrate, $CaSO_4\ {\bullet}2H_2O$) (PDF# 21-0816) and anhydrous sodium sulphate (PDF# 37-1465).

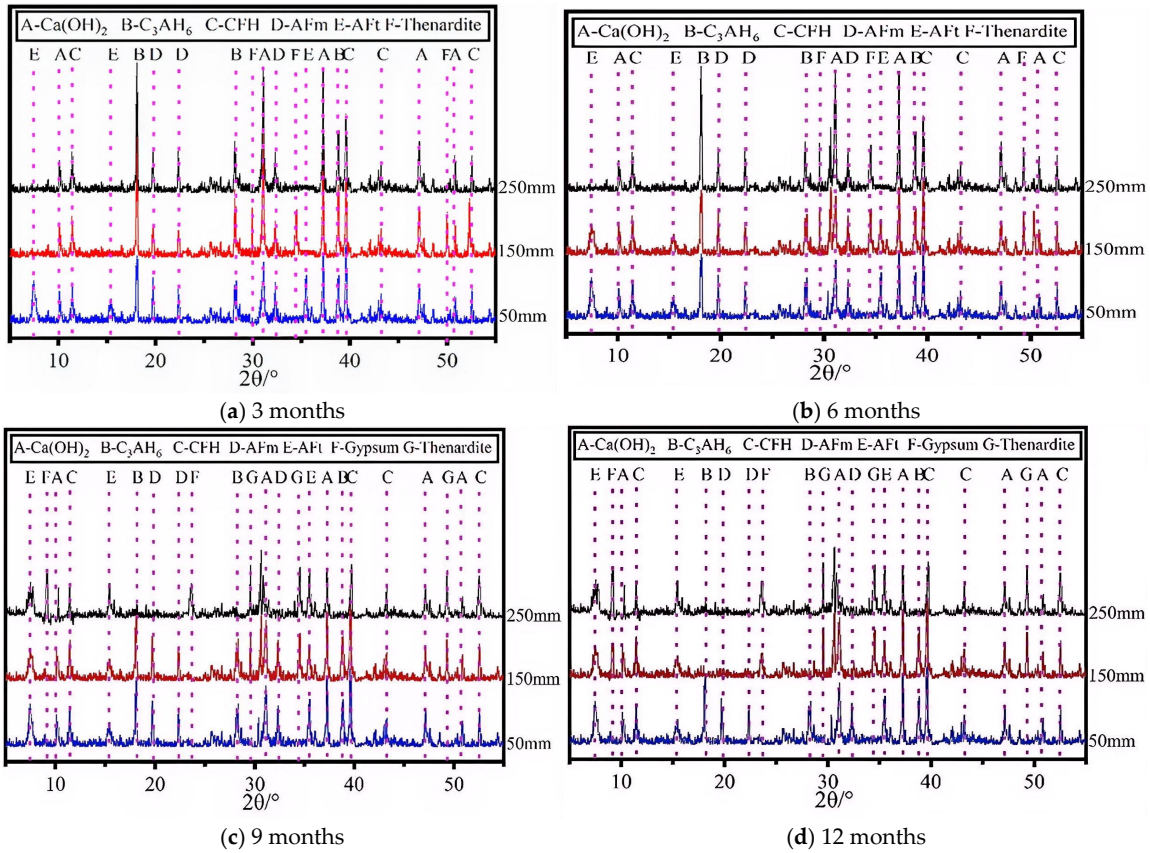

Figure 12. The XRD analysis results for different areas of C40 concrete.

The analysis of the XRD pattern for the corrosion after three months (Figure 12a) reveals that the primary mineral components in the half-immersed concrete in the Na_2SO_4 solution were $Ca(OH)_2$, C_3AH_6, AFm and CFH. A comparison revealed that the area 150 mm away from the specimen contained a higher concentration of the mineral anhydrous Na_2SO_4 and lacked the mineral component AFt, unlike the area 50 mm away from the specimen. Furthermore, the area 250 mm from the specimen height was devoid of the mineral composition AFt, compared to the area 50 mm from the specimen height. This result indicates that the Na_2SO_4 penetrating the concrete below the corrosion liquid level has reacted with the cement hydration products. The capillary action facilitates the upward transmission of Na_2SO_4, accumulating dehydrated Na_2SO_4 crystals on the specimen's surface. Given that the upward transmission of the Na_2SO_4 solution takes time, the primary mineral components near the top of the concrete specimen indicate no signs of corrosion deterioration in the upper part of the concrete specimen under the three months of corrosion.

Figure 12b–d demonstrates that anhydrous Na_2SO_4 gradually became evident in the area above the corrosion liquid level with increasing corrosion age. This outcome indicates that the Na_2SO_4 solution continues its upward transportation over time. The dehydration of $Na_2SO_4 \cdot 10H_2O$ in air leads to the ascension of a substantial amount of anhydrous Na_2SO_4 crystals along the concrete surface, resulting in the detection of significant quantities of anhydrous Na_2SO_4 in the area above the concrete liquid level. Moreover, the corrosion products gypsum and AFt progressively emerge in the mineral composition of concrete specimens in various areas. This finding indicates that chemical corrosion primarily occurs below the Na_2SO_4 semi-immersion corrosion liquid level, whereas the area above the liquid level experiences physical and chemical corrosion damage.

3.7. TG-DSC Analysis

Figure 13 depicts the TG-DSC curves for various areas of C40 concrete. The figure shows prominent $Ca(OH)_2$ mass loss peaks in the range of 400–500 °C [25,26]. At specimen heights of 50 mm, 150 mm and 250 mm, the weight loss rates of $Ca(OH)_2$ were 1.97%, 1.96% and 1.95%, respectively. With the increase in corrosion age, the weight loss rates of $Ca(OH)_2$ at these heights of C40 concrete remained within the ranges of 1.97–1.93%, 1.96–1.83% and 1.95–1.75%, respectively. This result indicates that the $Ca(OH)_2$ content in the area above the water level of semi-immersed Na_2SO_4 concrete was lower than that in the area below the water level. Moreover, regions closer to the top of the concrete exhibit lower $Ca(OH)_2$ content.

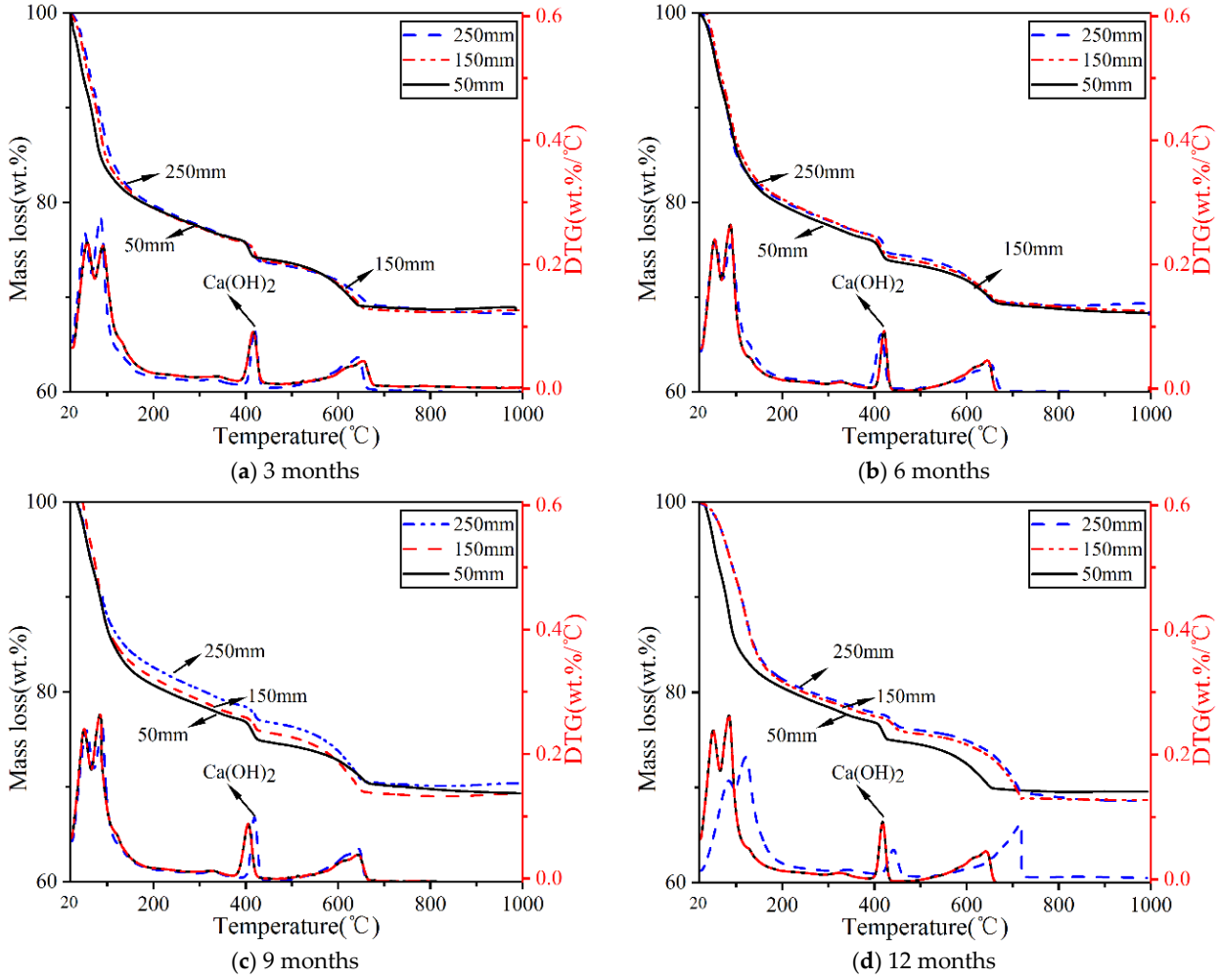

Figure 13. The TG-DSC curves for various areas of C40 concrete.

4. Migration and Capillary Rise of Sulphate Solution in Semi-Immersed Concrete

4.1. Distribution Characteristics of Concrete Semi-Immersed Corrosion Solution

The following mechanism analysis is established based on the experimental observations presented in Figures 1 and 2, which reveal the time-dependent evolution of sulphate solution seepage and surface climbing in C30 and C40 concretes. Figure 14a depicts that during the initial stages of corrosion in C30 concrete, the corrosion solution gradually permeates from the surface into the interior of the concrete in the soaked area. Because of the high pore connectivity in C30 concrete, sulphate, propelled by capillary forces, continuously moves upward through the internal pores of the concrete. This process results in sulphate transportation from the bottom to the upper part of the concrete. Accompanied by the infiltration of sulphate solution at the water level, the corrosion solution ascends along the concrete surface, elevating the wet zone's height. The concrete regions that remain unpenetrated by the sulphate attack solution consistently stay dry, constituting a dry zone in the concrete.

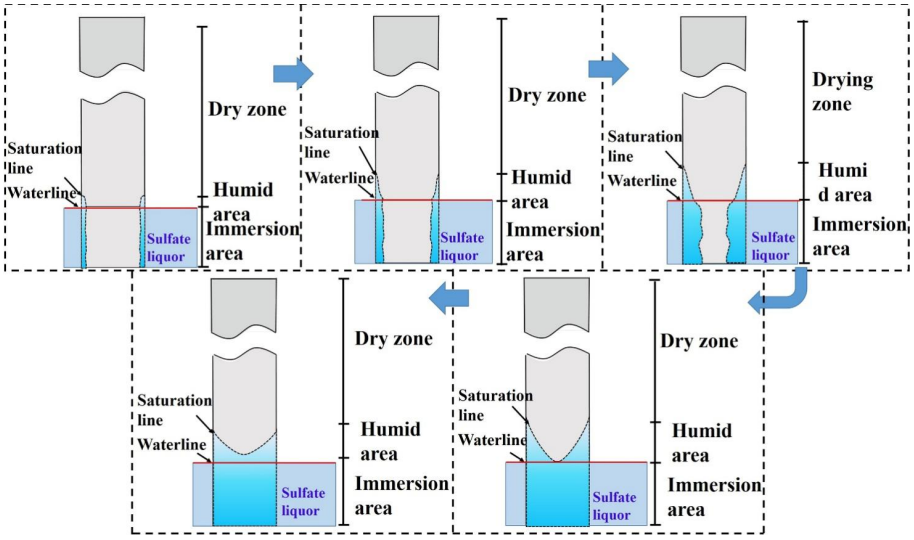

(**a**) Low-strength concrete

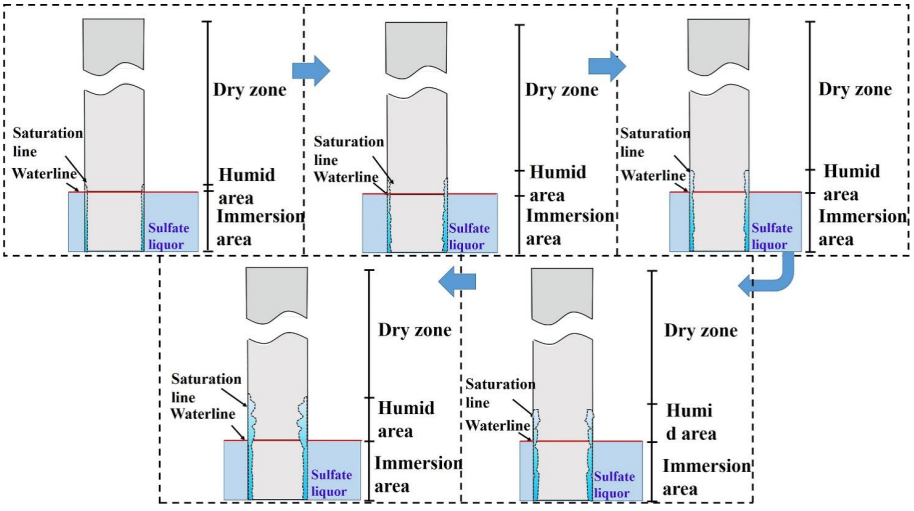

(**b**) C40 concrete

Figure 14. The distribution characteristics of the corrosion solution in the semi-immersed concrete.

During the intermediate stage of C30 concrete corrosion, the soaked area becomes thoroughly permeated by the sulphate corrosion solution as the soaking duration extends.

The rate at which the top of the corrosive solution rises is slower than the evaporation rate on the concrete surface, resulting in a convex formation at the top of the corrosive liquid. Due to the supersaturated sulphate state in this top area, the sulphate crystals undergo weathering and adhere to the concrete surface. In the later stages of C30 concrete corrosion, the upward migration height of sulphate, driven by capillary action, reaches its limit, stabilising the sulphate solution within the concrete at a specific height. However, the internal transmission rise within the concrete surpasses the external wetting climb height, leading to the seepage of liquid surface within the concrete, enveloping the liquid level of the external wetting climb.

Figure 14b illustrates the distribution characteristics of the corrosion solution in C40 concrete. In the sulphate attack's initial phase, the solution gradually seeps from the concrete surface into the interior within the soaking area. The concrete surface above the water level, influenced by sulphate infiltration, creates a wet zone of a certain height. During the intermediate stage of sulphate attack, sulphate infiltration extends from the surface to the interior of the concrete in the soaking area. Sulphate is continuously transported upward on the concrete surface due to capillary action, converging with the sulphate climbing on the surface, further elevating the wet zone's height. In the later stages of sulphate corrosion, the upward transmission of sulphate and the height of sulphate infiltration, driven by capillary action, reach their limits. Consequently, the wet zone on the concrete surface stabilises at a certain height, and the extent of the dry zone on the surface remains constant.

4.2. Surface Suction Climbing and Surface Calcium-Depleting Corrosion Mechanism in the Wet Zone Above the Water Level

Figure 15 shows the mechanism of surface suction climbing and surface alkali consumption corrosion in the wet zone above the water level. Figure 15a demonstrates the early stage of concrete corrosion. The concrete, semi-immersed in the sulphate solution, is stratified from bottom to top into several zones: submerged zone, wet zone, crystallization zone and dry zone. A closer examination of the wetted area at the concrete water level line reveals that the sulphate solution has thoroughly permeated this surface, creating a distinct wetted zone. Because of the ongoing water loss on the side of the humid area exposed to air, sulphate undergoes dehydration. It crystallises, subsequently accumulating in large quantities on the surface of the concrete specimen. Research indicates that the structure of concrete cement stone primarily comprises silicon-oxygen tetrahedral chains, calcium-oxygen layers and water molecules. As sulphate ascends from the concrete surface, a few SO_4^{2-} molecules integrate into the cement stone structure [31].

Figure 15b demonstrates the corrosion state of concrete in the mid-corrosion. It shows that as the duration of half-immersion in the sulphate corrosion solution lengthens, the extent and area of the concrete's wet and crystallisation zones expand. A minor degree of mortar spalling is observed in these zones. A closer examination of the dry–wet interface area reveals that, compared to the initial corrosion, the SO_4^{2-} concentration in this area progressively increases from the surface inward. The uneroded area gradually diminishes, whereas the impregnated area extends into the interior and exhibits a sandy region. Analysing the cement stone structure in the concrete surface area, it is evident that the accumulation of SO_4^{2-} within the cement stone structure reduces free Ca^{2+} content. This change causes the calcium–oxygen long-chain structure to bend, partially detaining the silicon-oxygen tetrahedra and rendering the cement stone structure unstable [32,33].

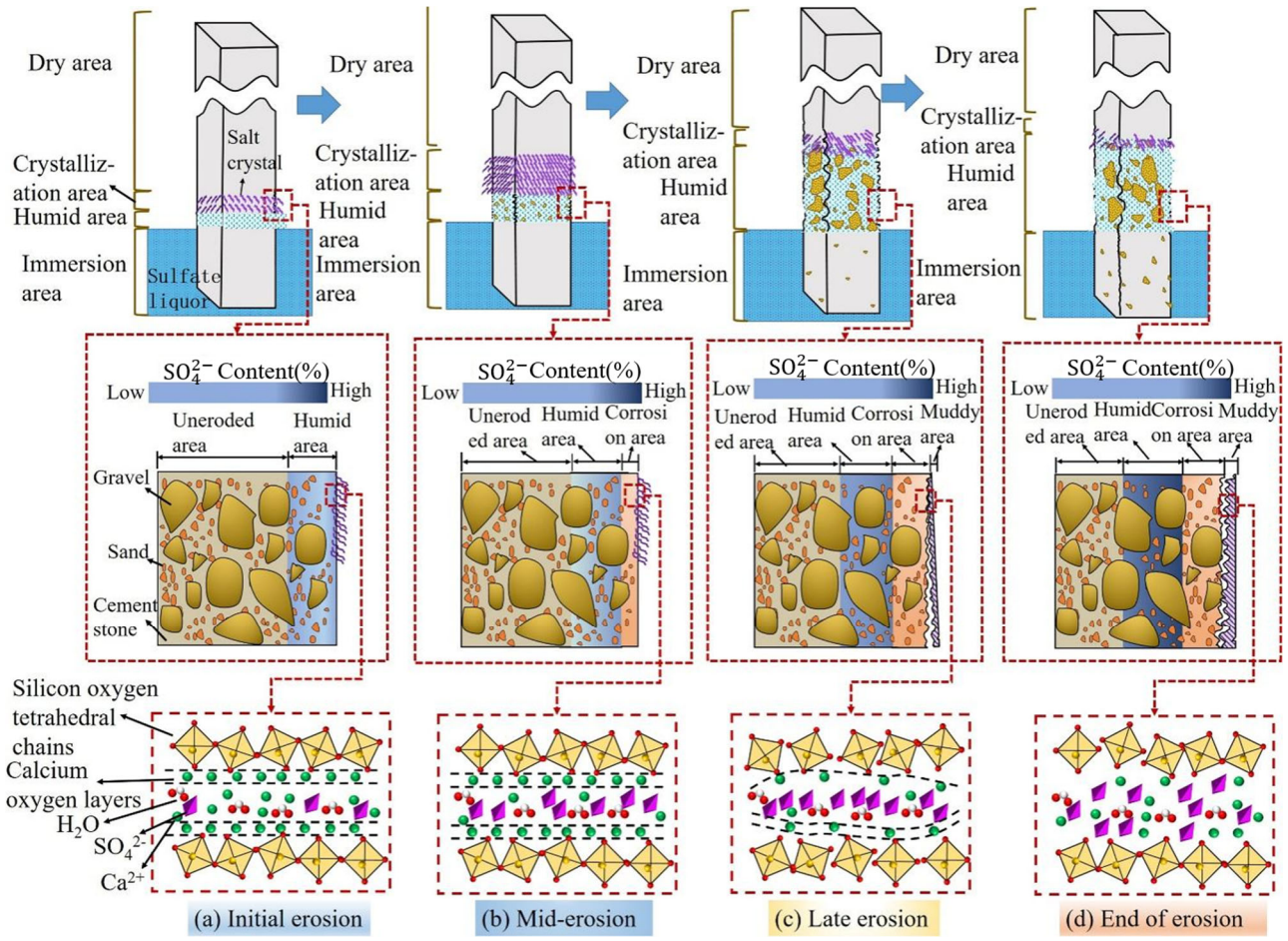

Figure 15. The mechanism of surface suction climbing and surface alkali consumption corrosion in the wet zone above the water level.

Figure 15c reveals the corrosion state of concrete in the later stages of corrosion, showing that as the duration of half-immersion in the sulphate corrosion solution increases, the uneroded area of the concrete transforms into wet area, with the crystallisation zone extending to the top of the concrete. In the uneroded area of the concrete, a large expanse of mortar has dislodged, and the mud has detached from the edges and corners of the concrete specimens. A detailed examination of the wet area along the water level line indicates that the SO_4^{2-} concentration in this region had progressed further into the concrete's interior than the initial stage of corrosion. The uneroded area has further diminished, with the moist and sandy areas advancing more profoundly into the concrete, accompanied by a muddy area. The analysis of the cement stone structure in the concrete surface area depicts a continual increase in the SO_4^{2-} content, leading to a partial disruption of the long-chain structure of the calcium-oxygen layer, thereby destabilising the cement stone structure.

Figure 15d illustrates the corrosion state of concrete at the end of corrosion, highlighting that with the intensification of sulphate corrosion, the phenomena of mortar peeling and muddying in the wet and crystallised areas of the concrete become more pronounced. The damage and peeling at the top of the concrete were particularly severe. A close examination of the wet area at the water level reveals that, compared to the middle stage of corrosion, the extent of the sandy and muddy areas continues to expand, with SO_4^{2-} encompassing the entire region. The analysis of the cement stone structure in the concrete surface area shows an incremental increase in SO_4^{2-} content. This increase in SO_4^{2-} leads to the disintegration and decomposition of the cement stone structure, primarily because of the dissolution and breakdown of Ca^{2+} in the calcium–oxygen layer's long-chain structure.

The waterline wet zone, due to sulphate climbing and supersaturation, suffers the earliest and most severe degradation, compromising structural integrity. Conventional protection is insufficient; interrupting the surface-climbing pathway is critical for durability. While the present analysis is primarily qualitative, future work will establish quantitative indices—such as normalized wet-zone area and sulphate penetration depth in the capillary rise region—to enable more rigorous characterization of sulphate migration and objective degradation assessment across concrete grades.

It should be noted that the modulus reduction of C-S-H gel observed by nanoindentation, while strongly correlated with sulphate exposure and $Ca(OH)_2$ depletion (as evidenced by XRD and TG-DSC), may not be attributed exclusively to chemical decalcification. Other concurrent processes, including microcracking induced by crystallization pressure of sulphate salts, porosity evolution due to dissolution of hydration products, and even ongoing hydration of residual cement clinker, could also contribute to the measured decrease in elastic modulus. Nevertheless, the spatial consistency between the reduction in C-S-H elastic modulus (nanoindentation) and the depletion of $Ca(OH)_2$ (TG-DSC) in the waterline wet zone, together with the appearance of gypsum and ettringite (XRD), strongly suggests that sulphate-induced decalcification of C-S-H is a primary driver of the observed mechanical degradation. The overall degradation is therefore interpreted as a multi-factor process, with chemical decalcification playing a central role, while microstructural damage (cracking and porosity increase) acts synergistically to accelerate the loss of structural integrity. Further direct compositional analysis is warranted in future work to definitively confirm the decalcification mechanism at the molecular level.

Furthermore, while this mechanistic study was conducted on plain Portland cement concrete to isolate the fundamental sulphate climbing and alkali-consumption degradation processes, future work should extend these findings to systems incorporating alternative binders and mineral additions (e.g., fly ash, slag, or limestone calcined clay), as their influence on matrix compactness and long-term resistance to sulphate attack in the waterline wet zone warrants systematic investigation.

5. Conclusions

(1) Under the action of surface tension, the concrete surface above the water line of the partially submerged component is gradually wetted, an erosion-wetting zone of a certain height at the water line. Although this zone is in an atmospheric environment, it is directly connected to the external water source of the zone, providing a pathway for the leaching of alkalis caused by sulphate attack on the concrete in this area.

(2) The sulphate solution climbs up along the surface to the wetting zone above the water line, leading to surface-downward alkali-leaching corrosion of the concrete in this zone, thereby causing the cracking and of the concrete.

(3) Under the action of surface tension, the sulphate solution continues to wet upwards to form a new erosion-wetting zone. With the continuous dissipation of mudding and upward erosion-wetting of the concrete surface, the erosion range of sulphates in the crystallization-wetting zone at the water line continuously expands.

(4) Traditional protective measures cannot provide long-term protection against sulphate erosion in the wetting zone at the water line. Cutting off the surface climbing path of sulphates in the wetting at the water line is expected to solve the long-term corrosion protection problem of the wetting zone at the water line. This is our next research goal.

(5) The waterline wet zone, due to sulphate climbing and supersaturation, suffers the earliest and most severe deterioration, compromising structural integrity. Conventional protection is insufficient; interrupting the surface-climbing pathway is critical for durability.

Author Contributions: J.D.: Writing—original draft, Methodology, Writing—review and editing. T.H.: Validation, Formal analysis. S.Z.: Visualization, Resources, Investigation. T.L.: Writing—review and editing, Methodology, Conceptualization. X.L.: Methodology, Investigation, Supervision. B.X.: Formal analysis, Validation. Y.Y.: Software, Visualization. Y.J.: Conceptualization, Validation. All authors have read and agreed to the published version of the manuscript.

Funding: This research was funded by the National Natural Science Foundation of China grant number (51972337).

Data Availability Statement: The original contributions presented in this study are included in the article.

Conflicts of Interest: Authors Junliang Dong, Xiaobo Liu, and Yang Yan were employed by Shenhua Group Xinjie Energy Co., Ltd. The remaining authors declare that the research was conducted in the absence of any commercial or financial relationships that could be construed as a potential conflict of interest.

References

1. Zhao, G.; Hu, Y.; Li, S.; Wang, Z.; Guo, M.; Han, F.; Wang, H. Degradation mechanisms of chloride contaminated cast-in-situ concrete partially exposed to magnesium-sulfate combined environment. *KSCE J. Civ. Eng.* **2023**, *27*, 618–629. [CrossRef]
2. Valuev, D.V.; Sharipzyanova, G.K.; Malsagov, B.S. Optimal Treatment of Coal Mine Wastewater Based on Settling Tanks. *Coke Chem.* **2024**, *67*, 615–620. [CrossRef]
3. Valuev, D.V.; Golik, V.I.; Israilov, R.Y. Optimal Settling Tank Treatment of Coal Mine Wastewater. *Coke Chem.* **2024**, *67*, 567–571. [CrossRef]
4. Kolesnyk, V.; Kulikova, D.; Kovrov, S. In-stream settling tank for effective mine water clarification. In *Annual Scientific-Technical Colletion—Mining of Mineral Deposits*; CRC Press: Boca Raton, FL, USA, 2013; pp. 285–289.
5. Yu, L.; Xia, J.; Gu, J.; Zhang, S.; Zhou, Y. Degradation Mechanism of Coal Gangue Concrete Suffering from Sulfate Attack in the Mine Environment. *Materials* **2023**, *16*, 3. [CrossRef] [PubMed]
6. Wang, Z.; Sun, P.; Zuo, J.; Liu, C.; Han, Y.; Zhang, Z. Long-term properties and microstructure change of engineered cementitious composites subjected to high sulfate coal mine water in drying-wetting cycles. *Mater. Des.* **2021**, *203*, 109610. [CrossRef]
7. Yu, L.; Chu, H.; Zhu, Z.; Jiang, L.; Dong, H. Determination of the chloride ion content in concrete under simultaneous chloride and sulphate ion attack. *J. Build. Eng.* **2023**, *72*, 106579. [CrossRef]
8. Liu, Z.; Zhu, J.; Yuan, Q.; Wang, C.; Zhang, F. Solution transportation in concrete partially exposed to Na2SO4 solution. *J. Sustain. Cem.-Based Mater.* **2020**, *9*, 371–381. [CrossRef]
9. Luo, Z.; Zhang, B.; Zou, J.; Luo, B. Sulfate corrosion resistance of slag-fly ash based geopolymer stabilized soft soil under semi-immersion condition. *Case Stud. Constr. Mater.* **2022**, *17*, e01506. [CrossRef]
10. Menéndez, E.; García-Rovés, R.; Aldea, B.; Ruíz, S.; Baroghel-Bouny, V. Combination of immersion and semi-immersion tests to evaluate concretes manufactured with sulfate-resisting cements. *J. Sustain. Cem.-Based Mater.* **2019**, *8*, 337–352. [CrossRef]
11. Zhao, G.; Guo, M.; Cui, J.; Li, J.; Xu, L. Partially-exposed cast-in-situ concrete degradation induced by internal-external sulfate and magnesium multiple coupled attack. *Constr. Build. Mater.* **2021**, *294*, 123560. [CrossRef]
12. Sun, H.; Liu, S.; Yu, F.; Zhang, X.; Wu, C.; Xing, F.; Ren, J. Behaviour of cement binder exposed to semi-immersion in chloride-rich salt solutions and seawater with different RH levels. *Cem. Concr. Compos.* **2022**, *131*, 104606. [CrossRef]
13. Esselami, R.; Wilson, W.; Tagnit-Hamou, A. An accelerated physical sulfate attack test using an induction period and heat drying: First applications to concrete with different binders including ground glass pozzolan and limestone filler. *Constr. Build. Mater.* **2022**, *345*, 128046. [CrossRef]
14. Genovés, V.; Vargas, F.; Gosálbez, J.; Carrión, A.; Borrachero, M.V.; Payá, J. Ultrasonic and impact spectroscopy monitoring on internal sulphate attack of cement-based materials. *Mater. Des.* **2017**, *125*, 46–54. [CrossRef]
15. Arel, H.Ş.; Thomas, B.S. The effects of nano- and micro-particle additives on the durability and mechanical properties of mortars exposed to internal and external sulfate attacks. *Results Phys.* **2017**, *7*, 843–851. [CrossRef]
16. Qiao, X.; Chen, J. Correlation of propagation rate of corrosive crack in concrete under sulfate attack and growth rate of delayed ettringite. *Eng. Fract. Mech.* **2019**, *209*, 333–343. [CrossRef]
17. Jiang, L.; Niu, D. Study of deterioration of concrete exposed to different types of sulfate solutions under drying-wetting cycles. *Constr. Build. Mater.* **2016**, *117*, 88–98. [CrossRef]
18. Jiang, J.; Tian, Y.; Lu, D.; Lu, X.; Ji, K.; Jia, K.; Zhang, J. Internal corrosion characteristics of endogenous sulfate introduced by recycled aggregates in recycled aggregates concrete: Insights into the macro-mechanical and meso-mechanical properties. *J. Clean. Prod.* **2023**, *426*, 139085. [CrossRef]

19. Santillán, L.R.; Villagrán Zaccardi, Y.A.; Zega, C.J.; Méndez, E.M. Macroscopic behavior and microstructural analysis of recycled aggregate mortar bars exposed to external sulfate attack. *Cem. Concr. Compos.* **2023**, *143*, 105277. [CrossRef]
20. Rirsch, E.; Zhang, Z. Rising damp in masonry walls and the importance of mortar properties. *Constr. Build. Mater.* **2010**, *24*, 1815–1820. [CrossRef]
21. Scherer, G.W. Stress from crystallization of salt. *Cem. Concr. Res.* **2004**, *34*, 1613–1624. [CrossRef]
22. Alyami, M.H.; Alrashidi, R.S.; Mosavi, H.; Almarshoud, M.A.; Riding, K.A. Potential accelerated test methods for physical sulfate attack on concrete. *Constr. Build. Mater.* **2019**, *229*, 116920. [CrossRef]
23. Girardi, F.; Vaona, W.; Di Maggio, R. Resistance of different types of concretes to cyclic sulfuric acid and sodium sulfate attack. *Cem. Concr. Compos.* **2010**, *32*, 595–602. [CrossRef]
24. Avet, F.; Scrivener, K. Influence of pH on the chloride binding capacity of limestone calcined clay cements (LC3). *Cem. Concr. Res.* **2020**, *131*, 106031. [CrossRef]
25. *GB 175-2023*; Common Portland Cement. State Administration for Market Regulation, Standardization Administration of China: Beijing, China, 2023.
26. *JGJ 52-2006*; Standard for Sand and Stone Quality and Inspection Methods for Ordinary Concrete. China Architecture & Building Press: Beijing, China, 2007.
27. *GB/T 13025.8-2012*; General Test Method in Salt Industry—Determination of Sulfate. Standards Press of China: Beijing, China, 2012.
28. *CECS 21:2000*; Technical Specification for Inspection of Concrete Defects by Ultrasonic Method. China City Press: Beijing, China, 2000.
29. Vandamme, M.; Ulm, F.-J. Nanogranular origin of concrete creep. *Proc. Natl. Acad. Sci. USA* **2009**, *106*, 10552–10557. [CrossRef] [PubMed]
30. Sebastiani, M.; Moscatelli, R.; Ridi, F.; Baglioni, P.; Carassiti, F. High-resolution high-speed nanoindentation mapping of cement pastes: Unravelling the effect of microstructure on the mechanical properties of hydrated phases. *Mater. Des.* **2016**, *97*, 372–380. [CrossRef]
31. Dolado, J.S.; Griebel, M.; Hamaekers, J. A Molecular dynamic study of cementitious calcium silicate hydrate (C–S–H) gels. *J. Am. Ceram. Soc.* **2007**, *90*, 3938–3942. [CrossRef]
32. Zhang, Z.; Ji, Y. Study on the deterioration mechanism of alkali dissolution of concrete mixed with Na2SO4 in external water source. *Constr. Build. Mater.* **2022**, *356*, 129283. [CrossRef]
33. Zhang, G.; Zhu, J.; Yang, J. Noscale insights on structure and properties of C-(A)-S-H gel in cementitious materials under sulfate attack. *Case Stud. Constr. Mater.* **2025**, *23*, e04981. [CrossRef]

Disclaimer/Publisher's Note: The statements, opinions and data contained in all publications are solely those of the individual author(s) and contributor(s) and not of MDPI and/or the editor(s). MDPI and/or the editor(s) disclaim responsibility for any injury to people or property resulting from any ideas, methods, instructions or products referred to in the content.